

The mean ultraviolet spectrum of a representative sample of faint $z \sim 3$ Lyman alpha emitters

Kimihiko Nakajima,^{1*}† Thomas Fletcher,² Richard S. Ellis,^{1,2} Brant E. Robertson³ and Ikuru Iwata⁴

¹European Southern Observatory, Karl-Schwarzschild-Str. 2, D-85748, Garching bei München, Germany

²Department of Physics and Astronomy, University College London, Gower Street, London WC1E 6BT, UK

³Department of Astronomy and Astrophysics, University of California, Santa Cruz, 1156 High Street, Santa Cruz, CA 95064, USA

⁴Subaru Telescope, National Astronomical Observatory of Japan, 650 North A'ohoku Place, Hilo, HI 96720, USA

Accepted 2018 March 17. Received 2018 February 23; in original form 2018 January 9

ABSTRACT

We discuss the rest-frame ultraviolet (UV) emission line spectra of a large (~ 100) sample of low luminosity redshift $z \sim 3.1$ Lyman alpha emitters (LAEs) drawn from a Subaru imaging survey in the SSA22 survey field. Our earlier work based on smaller samples indicated that such sources have high $[\text{O III}]/[\text{O II}]$ line ratios possibly arising from a hard ionizing spectrum that may be typical of similar sources in the reionization era. With optical spectra secured from VLT/VIMOS, we re-examine the nature of the ionizing radiation in a larger sample using the strength of the high ionization diagnostic emission lines of $\text{C III}] \lambda 1909$, $\text{C IV} \lambda 1549$, $\text{He II} \lambda 1640$, and $\text{O III}] \lambda \lambda 1661, 1666 \text{ \AA}$ in various stacked subsets. Our analysis confirms earlier suggestions of a correlation between the strength of $\text{Ly} \alpha$ and $\text{C III}]$ emission and we find similar trends with broad-band UV luminosity and rest-frame UV colour. Using various diagnostic line ratios and our stellar photoionization models, we determine both the gas phase metallicity and hardness of the ionization spectrum characterized by ξ_{ion} – the number of Lyman continuum photons per UV luminosity. We confirm our earlier suggestion that ξ_{ion} is significantly larger for LAEs than for continuum-selected Lyman break galaxies, particularly for those LAEs with the faintest UV luminosities. We briefly discuss the implications for cosmic reionization if the metal-poor intensely star-forming systems studied here are representative examples of those at much higher redshift.

Key words: galaxies: evolution – galaxies: high-redshift.

1 INTRODUCTION

A continuing debate in the high redshift community is whether early star-forming galaxies generate sufficient photons to govern the reionization process. The key questions relate to both the nature of the ionizing spectrum for low metallicity intensely star-forming systems thought to dominate the redshift interval $6 < z < 10$, and the extent to which the circumgalactic medium is transparent to Lyman continuum (LyC) radiation. Detailed diagnostics of these questions are currently challenging to observe for $z > 6$ sources. The nature of the ionizing spectrum, particularly the efficiency of the ionizing photon production from the stellar population defined by ξ_{ion} , the number of LyC photons per ultraviolet (UV) luminosity (e.g. Robertson et al. 2013), is ideally constrained by measures of Balmer emission (Bouwens et al. 2016) interpreted through re-

combination physics. However, the Balmer emission lines are currently beyond reach of ground-based telescopes at high redshifts. Furthermore, due to the rapid increase in intergalactic absorbers LyC leakage from galaxies at $z > 6$ cannot be directly measured (e.g. Madau 1995; Inoue & Iwata 2008; Inoue et al. 2014). For these reasons, attention has focused on identifying and studying possible analogues of low metallicity galaxies at low (e.g. Izotov et al. 2016a,b; Leitherer et al. 2016; Schaerer et al. 2016; Verhamme et al. 2017) and intermediate redshifts (e.g. Iwata et al. 2009; Nestor et al. 2013; Vanzella et al. 2016a,b; Amorín et al. 2017).

Low metallicity, low mass systems such as narrow-band selected Lyman alpha emitters (LAEs) at intermediate redshift may provide valuable examples of sources contributing to cosmic reionization. In a recent paper (Nakajima et al. 2016), we have demonstrated for a modest sample of 15 $z \sim 3$ LAEs that $[\text{O III}] \lambda \lambda 5007, 4959$ emission is unusually intense compared to $[\text{O II}] \lambda 3727$, contrary to similar measurements of the more metal rich Lyman break population (LBGs). We showed that this enhanced $[\text{O III}]$ is unlikely to be the result of a lower metallicity alone and may arise, at least

*E-mail: kimihiko.nakajima@nao.ac.jp

† JSPS Overseas Research Fellow

partially, from a harder ionizing spectrum. Since intense [O III] emission appears to be a common feature of sources in the reionization era, as inferred from *Spitzer*/IRAC broad-band photometry (Schenker et al. 2013; Smit et al. 2014, 2015; Roberts-Borsani et al. 2016), we argued that intrinsically faint $z \sim 3$ LAEs may be valuable analogues of the dominant population of faint sources which may govern reionization. Their importance in understanding the early universe also arises from the fact that the relative fraction of all star-forming galaxies showing strong Lyman alpha emission increases with redshift up to the reionization era (e.g. Stark, Ellis & Ouchi 2011; Curtis-Lake et al. 2012; Cassata et al. 2015).

In this paper, we attempt to further constrain the nature of the ionizing radiation, i.e. the efficiency of the LyC photon production characterized by ξ_{ion} , for a much larger sample of ~ 100 $z \sim 3$ LAEs drawn from the same parent data set as in Nakajima et al. (2016) via constraints on the strength of high ionization UV metal lines, principally C III] $\lambda 1909$ and C IV $\lambda 1549$, which are redshifted into the optical at $z \simeq 3.1$.¹ This approach follows a similar analysis undertaken for sub-luminous lensed Lyman break galaxies (LBGs) at $z \sim 2-3$ (Stark et al. 2014) interpreted with photoionization codes (e.g. Nakajima & Ouchi 2014; Feltre, Charlot & Gutkin 2016; Gutkin, Charlot & Bruzual 2016; Nakajima et al. 2017), which also supported the notion of a harder ionizing radiation field compared to local sources.

A plan of the paper follows. In Section 2, we introduce the sample targeted for follow-up spectroscopy which is drawn from a field previously surveyed with narrow-band filters with the Subaru telescope. We discuss the observations undertaken with both the Keck and ESO VLT telescopes and the techniques used to reduce these data. In Section 3, we discuss the spectroscopic results in terms of the success rates of recovering Ly α emission in the two observational campaigns and the velocity offset of Ly α , $\Delta v_{\text{Ly}\alpha}$, relative to the systemic velocity inferred from nebular lines. The relationship between $\Delta v_{\text{Ly}\alpha}$ and the equivalent width [EW(Ly α)] is then used to stack the higher quality ESO spectra in various ways. Furthermore, we interpret these spectroscopic stacks and provide constraints on the ratios of various UV metal lines, which we interpret with photoionization models thereby deriving measures of the gas phase metallicity and hardness of the ionizing spectrum. We discuss the implications of our results and present a summary in Section 4.

We assume a Lambda cold dark matter cosmology using the Planck results with $\Omega_{\text{M}}=0.308$, $\Omega_{\Lambda}=0.692$, and $H_0=67.8 \text{ km s}^{-1} \text{ Mpc}^{-1}$. We adopt a solar chemical composition following Asplund et al. (2009).

2 SPECTROSCOPIC DATA

2.1 Sample

Our target sample of $z \sim 3.1$ LAEs is drawn from earlier panoramic narrow-band imaging surveys undertaken with the Subaru Telescope. In our previous paper (Nakajima et al. 2016, hereafter Paper I), we secured near-infrared spectra sampling [O II], H β , and [O III] emission for 15 sources in the SSA22 field (Hayashino et al. 2004; Yamada et al. 2012; Micheva et al. 2017) using Keck/MOSFIRE. 13 of these 15 objects are LAEs with EW(Ly α) $> 20 \text{ \AA}$ and the remaining two are LBGs also at $z \simeq 3.1$. The present

enlarged sample is drawn from 281 LAEs in the same field (SSA22-Sb1; Yamada et al. 2012) including the 13 MOSFIRE-identified LAEs selected via their photometric excess in a narrowband filter centred at 497 nm. In order to obtain rest-frame UV spectra to further our studies of the nature of this population, we conducted deep optical spectroscopy of a subset of these photometrically identified LAEs using the VLT/VIMOS spectrograph. Optical spectroscopy was also obtained using the Keck/LRIS spectrograph in a second SXDS field for which MOSFIRE data is available (Fletcher et al., in preparation). That data is only used here to enlarge the sample for which Ly α velocity offsets can be determined (Section 3.1).

In the VIMOS sample, we secured UV spectra for 7 of the 13 LAEs and one of the two LBGs in the SSA22 field for which MOSFIRE spectra are available from Paper I. Additionally, we sampled a further 77 LAEs and 12 LBGs. In total, our new enlarged sample of rest-frame optical spectroscopy comprises 84 LAEs and 13 LBGs, representing a considerable advance over the sample discussed in Paper I. Finally, we have likewise recently enlarged the sample for which MOSFIRE near-infrared spectra is available (Nakajima et al., in preparation). This data provides new rest-frame optical emission lines for 6 LAEs and 2 LBGs and is also used only here to improve our understanding of the Ly α velocity offsets (Section 3.1). Further details of the observations are given in the following subsection.

An important advantage of selecting the SSA22 field is the plentiful deep multiwavelength photometric data. The optical broad-band data is useful in constraining the nature of the stellar populations, such as the absolute UV magnitude M_{UV} and the UV continuum slope parameter β . We derive the absolute UV magnitude using R -band photometry which traces the rest frame spectral energy distribution (SED) around 1500–1600 \AA , and the UV continuum slope β is measured assuming a power-law fit to the R , i , and z -band photometry according to the convention $f_{\lambda} \propto \lambda^{\beta}$. Such β measurements are thus possible only for those LAEs detected in at least two of the Subaru R , i , and z -band images. A resulting distribution of the UV slope is $\beta \simeq -1.6 \pm 0.8$, which corresponds to $E(B - V) \simeq 0.09 \pm 0.07$ with the SMC extinction curve and the BPASS SEDs (Reddy et al. 2018). This is comparable to the results of other photometric studies of LAEs at similar redshifts, where β values are calculated as in Meurer et al. (1997) (e.g. Nilsson et al. 2009) and $E(B - V)$ via SED fitting analysis (e.g. Ono et al. 2010; Guaita et al. 2011; Nilsson et al. 2011; Kusakabe et al. 2018). Finally, although the VIMOS spectra are crucial in confirming the Ly α emission, they cannot provide accurate measures of the EW of Ly α due to the low signal-to-noise ratio (S/N) of the UV continuum and aperture effects inevitable with slit spectroscopy (e.g. Momose et al. 2016; Wisotzki et al. 2016). It is preferable, therefore, to measure EWs of Ly α from the BV – NB497 colours, where BV stands for a combination of the B and V broad-band images as $(2B+V)/3$ (Hayashino et al. 2004). This can be done by using the Ly α observed wavelength in the EW calculation and taking into account the narrow-band and broad-band filter transmission curves to accurately translate the BV – NB497 colour into the EW. The limiting depths of the relevant broad-band photometry in the SSA22 field are given in Table 1.

It is useful to compare the properties of our new spectroscopic sample with those for which similar line emission studies have been undertaken. Fig. 1 compares the UV luminosity distribution of our 97 targets with those for other $z \simeq 2-3$ star-forming galaxies (Shapley et al. 2003; Erb et al. 2014; Stark et al. 2014). Our LAE sample probes a M_{UV} range from -22.4 down to -18.7 with a median value of -19.5 . Notably, 15 of our LAEs are fainter than the broad-band detection limit ($M_{\text{UV}} \gtrsim -18.7$) and the 800 or so UV-selected LBGs

¹ The C III] $\lambda 1909$, or simply C III], refers to the sum of the [C III] $\lambda 1907$ and [C III] $\lambda 1909$. The C IV $\lambda 1549$, or C IV, quotes the C IV doublet of $\lambda = 1548$ and 1550 \AA .

Table 1. Summary of optical imaging data.

Band	Field	Observatory	PSF (1)	m_{lim} (2)	Reference (3)
<i>NB497</i>	SSA22	Subaru	1.0	26.2	(a), (b), (c)
<i>B</i>	SSA22	Subaru	1.0	26.5	(a), (b), (c)
<i>V</i>	SSA22	Subaru	1.0	26.6	(a), (b), (c)
<i>R</i>	SSA22	Subaru	1.1	26.7	(a), (c)
<i>i'</i>	SSA22	Subaru	1.0	26.4	(a)
<i>z'</i>	SSA22	Subaru	1.0	25.7	(a)

Notes. (1) full width at half-maximum in arcsec. (2) 5σ limiting magnitude estimated by 2 arcsec diameter aperture photometry. (3) (a) Hayashino et al. (2004); (b) Yamada et al. (2012); and (c) Matsuda et al. (2004).

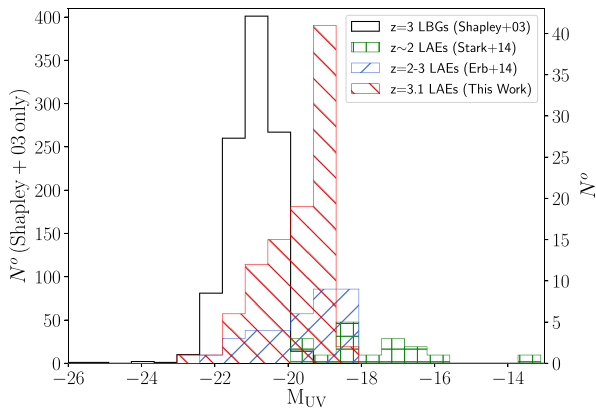


Figure 1. UV absolute magnitude distributions for recently published rest-frame UV spectroscopic studies at $z = 2-4$. Our VIMOS sample is plotted with the red hatched histogram. Other data sets include LBGs: Shapley et al. (2003) in black (numbers in the left-hand ordinate) and Erb et al. (2014) in blue, and gravitationally lensed galaxies from Stark et al. (2014) in green.

from Shapley et al. (2003) with $R \sim 24.4-24.9$, corresponding to M_{UV} of -21.1 to -20.6 . Only the 16 gravitationally lensed galaxies at $z = 1.6-3$ studied by Stark et al. (2014) overlaps our luminosity range. That sample extends from $M_{\text{UV}} = -19.9$ down to -13.7 .

2.2 VIMOS observations

The VIMOS spectroscopic observations were undertaken in the SSA22 field on UT3 of the VLT in Service Mode (ID: 098.A-0010(A), PI: Ellis) in August–October 2016. A single VIMOS pointing was adopted, comprising a slit mask across four quadrants of the instrument with a field of view of $4 \times 7 \text{ arcmin} \times 8 \text{ arcmin}$. To mitigate atmospheric dispersion, the slitlet position angle is restricted to $\text{PA} = 90^\circ$ and the field centre was chosen to maximize the number of targets for which $[\text{O III}]\lambda 5007$ had been detected already with MOSFIRE (Paper I). Seven LAEs and one LBG from Paper I fell in one quadrant (# 3) and the remaining sample totalling 97 sources included 77 new LAEs at $z = 3.1$ and 12 LBGs at $z = 3-4$ as well as the eight MOSFIRE objects. The new sample of 77 LAEs was drawn uniformly from the parent catalogue and has a median M_{UV} of -19.5 .

We observed in medium-resolution mode with the GG475 order sorting filter which provided a wavelength coverage from $\sim 4800 \text{ \AA}$ to $\sim 1 \mu\text{m}$ at a mean spectral resolution of $R \sim 580$ with a slit width of 1 arcsec. Our observation comprised 13 identical observing blocks (OBs), each with an on-source integration of $3 \times 20 \text{ min}$ using a three point offset pattern along the slit. Relatively bright stars were included on each quadrant adopted to monitor sky conditions and

mask alignment. Two of the 13 OBs were discarded as the seeing inferred was $\gtrsim 1$ arcsec. For quadrant #4, the first five OBs, one of which was under a poor seeing condition, were lost due to either an improper alignment or mis-insertion of the milled mask. The other three quadrants in these five OBs were unaffected, since mask alignment was performed excluding the alignment stars in quadrant #4. We thus discarded four additional OBs' data for quadrant #4.

In summary, therefore, we obtained in total 11 hr of on-source integration data for objects in the quadrants #1, 2, and 3, and 7 hr in the quadrant #4. The typical seeing for the acceptable OBs was 0.75 arcsec.

The VIMOS data was reduced using recipes in the standard ESO VIMOS pipeline (v.3.1.7) operated through ESOREFLEX (v.2.8.5). For each OB, the process included bad pixel cleaning, bias subtraction, flat-field correction, frame combination, sky fringing correction, wavelength calibration, and flux calibration. We performed wavelength calibration and flat-field using relevant frames taken after each OB. Using the slit position of each science target output by the VIMOS pipeline, we extracted the individual 2D spectrum. Sky subtraction was performed with a low-order polynomial fit along the slit for each wavelength. The 2D spectra were corrected for Galactic extinction based on the $E(B - V)$ map of Schlegel, Finkbeiner & Davis (1998). Finally, we combined the individual sky-subtracted 2D spectra ($N = 11$ for objects in the quadrants #1, 2, and 3, and $N = 7$ in the quadrant #4) with a sigma-clipped average to produce a final 2D spectrum for each of the science targets. 1D spectra were produced for those targets for which at least one emission line could be identified (normally $\text{Ly}\alpha$) adding up 9 pixels along the spatial direction centred on the detected emission line. This width was chosen to maximize the S/N and corresponds approximately to twice the seeing size.

2.3 Spectroscopic confirmations

Our initial task is to spectroscopically confirm the validity of the photometric identifications of $\text{Ly}\alpha$ emission at the expected redshift of $z \simeq 3.1$. Earlier work drawn from the same Subaru narrow-band imaging survey (Hayashino et al. 2004) has found a typical success rate of $\simeq 66$ per cent (Matsuda et al. 2005) (see Section 3.1). Initially therefore, two authors independently examined the VIMOS spectra for detectable $\text{Ly}\alpha$ emission through visual inspection of both the 1-D and 2-D spectra separately. Such an approach was considered adequate given that the wavelength of $\text{Ly}\alpha$ emission is accurately predicted by the narrowband filters.

Applying a 3σ S/N limit for the line detections, this investigation resulted in a confirmed list of 65 $z = 3.1$ LAEs corresponding to a relative success rate is 77 per cent ($=65/84$). Fig. 2 shows the success rate as a function of M_{UV} and $\text{EW}(\text{Ly}\alpha)$. Notably, we recover $\text{Ly}\alpha$ emission spectroscopically for 100 per cent of those LAEs with $\text{EW}(\text{Ly}\alpha) > 60 \text{ \AA}$. The success rate is higher than reported by Matsuda et al. (2005) (66 per cent). We consider this reasonable because (i) our VIMOS observations are deeper than earlier studies, and (ii) our sample probes fainter sources. Among the 16 objects studied with MOSFIRE, both in Paper I and with our most recent campaign (Nakajima et al., in preparation.), 12 show $\text{Ly}\alpha$ emission in the VIMOS spectrum.

From our VIMOS observations we also find 2 out of 13 LBGs show prominent $\text{Ly}\alpha$ emission with rest-frame EW of $> 20 \text{ \AA}$. Hereafter, we will refer to these 2 LBGs and the 65 genuine LAEs observed as the ‘VIMOS-LAEs’. We are confident that such sources cannot be explained as lower- z emitters, such as $[\text{O II}]\lambda 3727$ emitters at $z \simeq 0.3$ and $\text{H}\beta$ -or- $[\text{O III}]$ emitters at $z \lesssim 0.03$ because

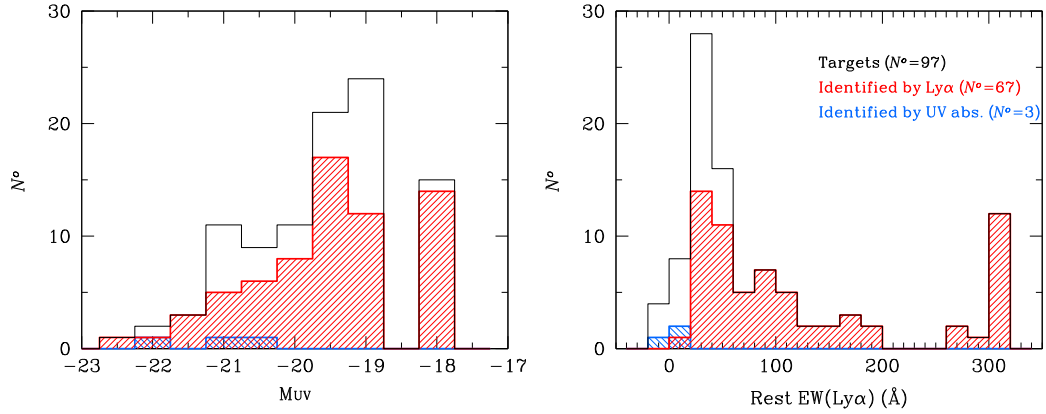


Figure 2. Distributions of M_{UV} (left-hand panel) and $EW(Ly\alpha)$ (right-hand panel) for the VIMOS sample. Red hatched histograms show the numbers of galaxies whose $Ly\alpha$ is spectroscopically confirmed, and the blue histogram presents LBGs identified via UV absorption line(s). LAEs whose UV continuum was not detected in the Subaru images are assigned to $M_{UV} > -18.5$ and $EW(Ly\alpha) > 300\text{ \AA}$.

Table 2. Summary of the VIMOS observation for the $z = 3.1$ LAEs.

Instrument	Field	Date of observation	Exposure times (hrs)	Wavelength coverage (\AA)	R	N^o of LAEs [LBGs] ^(†)	
						Observed	Identified
VIMOS	SSA22	2016 Aug & Oct	11.0 (quads. #1–3) 7.0 (quad. #4)	4850–9450	580	72 [10] 12 [3]	59 [1] ^(‡) 6 [1]

Notes. (†) Numbers of LBGs are given in the square brackets. (‡) Three additional LBGs that lack $Ly\alpha$ emission are identified with UV absorption lines.

of the lack of stronger emission lines of $[O\text{III}]\lambda 5007$ and $H\alpha$ at the corresponding wavelengths.

At this stage, prior to stacking the VIMOS spectra (Section 3.2), we also inspected the individual spectra searching for other emission lines. Among the 67 VIMOS-LAEs, only 15 sources reveal additional UV metal lines including: $C\text{III}]\lambda 1909$, $O\text{III}]\lambda 1665$, $He\text{II}]\lambda 1640$, and/or $C\text{IV}]\lambda 1549\text{ \AA}$. Most of these sources (10/15) present only $C\text{III}]\lambda$ emission with a tentative detection of the other UV line(s). These sources are generally the brighter subset in the spectroscopic sample, including one galaxy initially selected as a LBG and one LAE known as a TypeII AGN (Paper I). We additionally find 3 LBGs whose $Ly\alpha$ emission is not visible but for which UV absorption lines are detected.

We can now summarize the fruits of our spectroscopic campaign for a total of 97 targets (see Table 2). The catalogue summarizing which sources have individual metal line detections is provided in Table 3.

3 RESULTS

3.1 $Ly\alpha$ emission and its velocity offset

The overlap of 12 confirmed LAEs with our earlier MOSFIRE data (Paper I plus Nakajima et al., in preparation.) and our new $Ly\alpha$ detections from both VIMOS and LRIS (Fletcher et al., in preparation) enables us to revisit the question of the velocity offset of $Ly\alpha$, $\Delta v_{Ly\alpha}$, with respect to other nebular lines. This offset is crucial to understand prior to stacking spectra in order to achieve reliable detection of weaker UV metal lines. Traditionally, this quantity has been investigated as a function of the EW of $Ly\alpha$ (Adelberger et al. 2003) and we examine this relationship anew combining both literature data (Erb et al. 2014; Shibuya et al. 2014; Song et al. 2014; Trainor et al. 2015; Erb et al. 2016; Yang et al. 2017) and our own SSA22 measures in Fig. 3. As discussed in Section 2.1 and above,

we bring into play both the LRIS and recent MOSFIRE data only for the purpose of increasing the sample size.

Examination of this data suggests a new relationship given by:

$$\begin{aligned} \Delta v_{Ly\alpha} \text{ (km s}^{-1}\text{)} &\simeq 150 && \text{(EW} > 70\text{ \AA)} \\ &\simeq 360 - 3\text{ EW} && \text{(EW} = 20\text{--}70\text{ \AA)} \\ &\simeq 600 - 15\text{ EW} && \text{(EW} < 20\text{ \AA)}. \end{aligned} \quad (1)$$

Such an anticorrelation between $EW(Ly\alpha)$ and $\Delta v_{Ly\alpha}$ has been previously reported in data sets with a wide dynamic range in $EW(Ly\alpha)$ (e.g. Hashimoto et al. 2013; Erb et al. 2014; Shibuya et al. 2014; Trainor et al. 2015). As discussed by earlier kinematic studies of LAEs, the column density of H I gas must play a key role in shaping the anti-correlation, with a larger offset from systems of a higher column density. By combining all the individual data points from the literature, we confirm that the correlation becomes steeper towards a smaller $\Delta v_{Ly\alpha}$, i.e. that the spread in EW distribution increases with a smaller $Ly\alpha$ velocity offset. This trend is as theoretically expected (e.g. Zheng & Wallace 2014), as the secondary effects of anisotropy of the system and viewing angle become less significant in a higher column density. We cannot however fully examine the relationship for LAEs with $EW(Ly\alpha) \gtrsim 100\text{ \AA}$ due to the modest sample size, and thus present an average velocity offset of $\Delta v_{Ly\alpha} \simeq 150\text{ km s}^{-1}$ for such strong LAEs. The kinematics properties of our LAEs will be discussed in more detail elsewhere. The relation of equation (1) appears to be more appropriate than that presented by Adelberger et al. (2003), especially for galaxies showing strong $Ly\alpha$ emission. We investigate the difference between both relationships in our stacking analysis below.

3.2 Stacked spectra

Despite our significant integration time, we only directly detect other UV emission lines in a small subset of our data (Section 2.3,

Table 3. Properties of the VIMOS-LAEs with UV-line detection.

Objects	R.A. (1)	Dec. (1)	M_{UV} (2)	$EW(Ly\alpha)$ (\AA) (3)	$z_{Ly\alpha}$ (4)	$\Delta v_{Ly\alpha}$ (km s^{-1}) (5)	β (6)	UV line(s) (7)
– NB497-selected –								
LAE86177	22:16:47.6	+00:17:51	-19.3 ± 0.2	111^{+33}_{-26}	3.0734	–	$-2.32^{+0.68}_{-0.82}$	CIII], OIII](\dagger)
LAE104812	22:16:48.9	+00:21:41	-20.3 ± 0.1	23^{+6}_{-5}	3.0967	–	–	CIII], OIII](\dagger), HeII(\dagger)
LAE82902	22:16:59.6	+00:17:16	-20.1 ± 0.1	120^{+15}_{-13}	3.0717	–	$-1.50^{+0.34}_{-0.34}$	CIII], OIII](\dagger), HeII(\dagger)
LAE104037	22:17:06.7	+00:21:33	-21.4 ± 0.1	36^{+2}_{-2}	3.0673	+194	$-1.62^{+0.08}_{-0.18}$	CIII], OIII], HeII
LAE94460	22:17:08.0	+00:19:32	-19.9 ± 0.1	51^{+8}_{-7}	3.0744	+171	$-1.96^{+0.40}_{-0.36}$	CIII], OIII](\dagger)
LAE96549	22:17:26.3	+00:19:58	-19.5 ± 0.2	77^{+3}_{-3}	3.0455	–	$-2.44^{+1.26}_{-1.50}$	CIII]
LAE84811	22:17:27.8	+00:17:37	-19.0 ± 0.3	270^{+101}_{-69}	3.0928	–	$-1.20^{+1.04}_{-0.98}$	CIII]
LAE46348	22:17:30.4	+00:09:06	-22.4 ± 0.1	20^{+7}_{-7}	3.1500	–	$-0.96^{+0.04}_{-0.04}$	CIII], CIV(+abs.)
LAE105870	22:17:33.3	+00:21:51	-19.4 ± 0.2	138^{+49}_{-35}	3.0933	–	$-3.76^{+1.46}_{-0.24}$	CIII]
LAE52973	22:17:38.9	+00:11:02	-21.0 ± 0.1	81^{+7}_{-6}	3.0654	–	$-1.42^{+0.10}_{-0.26}$	CIII], HeII(\dagger)
LAE104357	22:17:42.6	+00:20:55	-21.8 ± 0.1	97^{+3}_{-3}	3.1732	–	$-1.72^{+0.12}_{-0.10}$	CIII], CIV(+abs.), HeII
LAE65130	22:17:48.7	+00:13:33	-20.2 ± 0.1	412^{+64}_{-53}	3.0565	–	$-1.34^{+0.36}_{-0.34}$	CIII]
LAE52126	22:17:56.4	+00:10:44	-19.7 ± 0.2	56^{+13}_{-11}	3.1230	–	$-1.18^{+0.44}_{-0.54}$	CIII](\dagger), OIII](\dagger)
AGN86861	22:17:09.6	+00:18:01	-21.5 ± 0.1	82^{+3}_{-2}	3.1097	+338	$-2.38^{+0.08}_{-0.22}$	CIV, HeII, NV, HeII, CIII]
– UV-selected –								
LAE50416	22:17:08.1	+00:09:58	-21.1 ± 0.1	117^{+3}_{-3}	3.2911	–	$-1.96^{+0.24}_{-0.28}$	CIII], OIII], CIV, HeII(\dagger)

Notes. (1) Coordinates are in J2000. (2) Absolute UV magnitude. (3) Rest $EW(Ly\alpha)$. For the NB497-selected LAEs, the EW is estimated from the BV–NB497 colour in conjunction with the $Ly\alpha$ redshift. The EW of UV-selected galaxy of LAE50416 is derived from spectroscopy. (4) Redshift determined with $Ly\alpha$. (5) Velocity offset of $Ly\alpha$. The systemic redshift is determined by the rest-frame optical emission lines provided by the MOSFIRE observation (Paper I). (6) UV continuum slope β . (7) UV emission line(s) except for $Ly\alpha$ identified with VIMOS. (\dagger) Tentative detection.

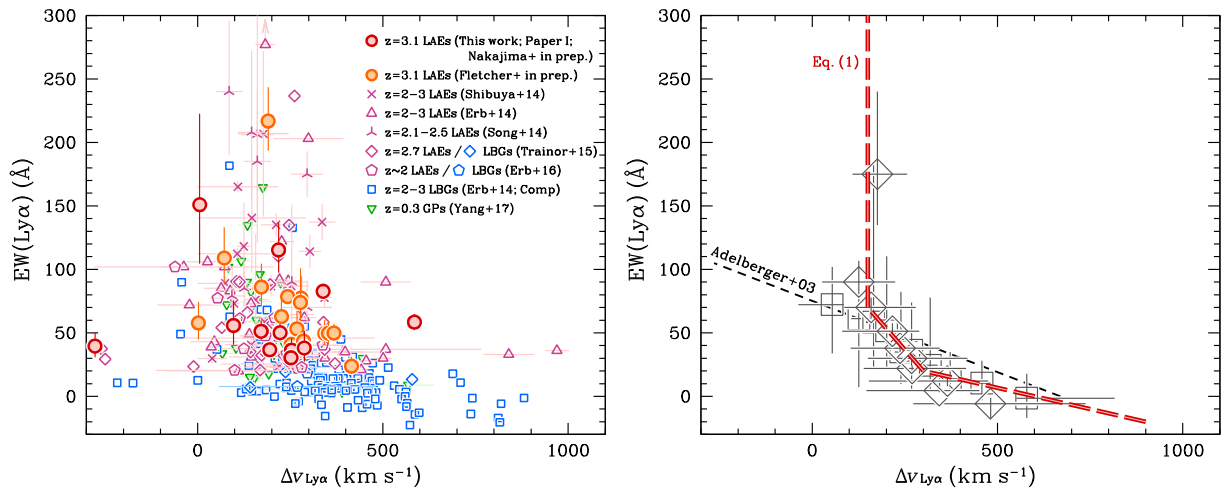


Figure 3. Left-hand panel: relationship between $EW(Ly\alpha)$ and the velocity offset $\Delta v_{Ly\alpha}$ for the VIMOS and other samples. Red filled circles represent the newly observed LAEs with VIMOS whose systemic redshift is determined using MOSFIRE detections of [O III] (Paper I). Orange circles show those additional LAEs observed with LRIS and recent MOSFIRE data (see the text for details). Magenta, blue, and green symbols represent equivalent measures for high redshift LAEs, LBGs with weak $Ly\alpha$ ($EW < 20 \text{\AA}$), and low- z green pea galaxies, respectively (see legend). Right-hand panel: open grey squares present the average $EW(Ly\alpha)$ for a $\Delta v_{Ly\alpha}$ bin, and open grey diamonds show the average $\Delta v_{Ly\alpha}$ for a $EW(Ly\alpha)$ bin, using all the individual data points shown in the left-hand panel. The red long-dashed lines is the derived relationship based on equation (1), while the black dashed line shows that from Adelberger et al. (2003).

Table 3). To determine the average strengths of CIII] and other diagnostic UV metal lines, we adopted the following stacking procedure.

First, we removed the single known active galactic nucleus (AGN; Section 2.3) from the sample leaving 66 VIMOS-LAEs. Additionally, since their rest-frame optical lines are identified, we included those four targets confirmed with MOSFIRE for which $Ly\alpha$ is not

visible in the VIMOS spectrum. The sample available for stacking analyses thus consists of 70 sources.

Using the individual flux-calibrated spectra, we shifted each to the rest-frame as described below, rebinned each to a common dispersion of 0.65\AA per pixel, and scaled to a common median in the wavelength range of $\sim 1250\text{--}1500 \text{\AA}$. Finally, the spectra were averaged. To exclude positive and negative sky subtraction

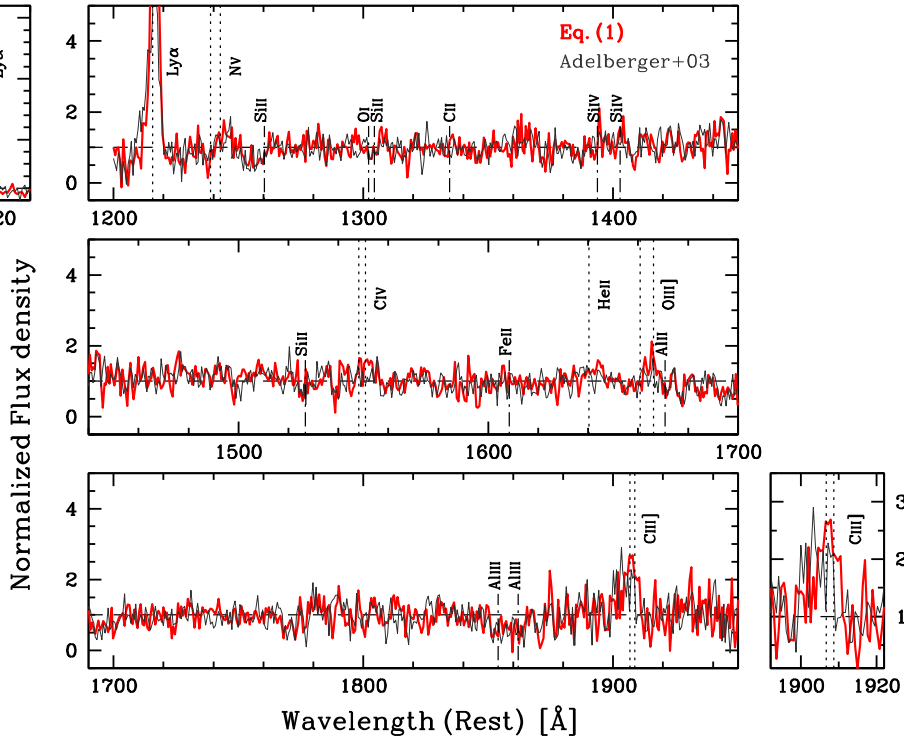


Figure 4. The normalized composite rest-frame spectrum for the sample of 70 spectroscopically confirmed VIMOS LAEs. The thick red spectrum adopts the relationship between $\Delta v_{\text{Ly}\alpha}$ and $\text{EW}(\text{Ly}\alpha)$ that we derive with the latest compilation of LAEs and LBGs (i.e. equation 1), while the thin black is based on the Adelberger et al. (2003) relation. Additional panels focus on the $\text{Ly}\alpha$ and C III] emission regions and highlight the difference between the two methods. Wavelengths of additional emission lines and absorption lines are marked with a dotted and dot-dashed vertical line, respectively.

residuals and cosmic ray residuals, we rejected an equal number of the highest and lowest outliers at each wavelength corresponding in total to ~ 5 per cent of the data. We confirmed that median-stacked composite spectra generated in the same way were almost indistinguishable from the average-stacked ones.

To define a systemic redshift for each galaxy, we adopted a similar approach used by Shapley et al. (2003). We used the rest-frame optical redshifts for the MOSFIRE identified objects in SSA22 (Paper I; Nakajima et al., in preparation). For the others, we estimated a systemic redshift from the $\text{Ly}\alpha$ using the updated formula given by equation (1).

The normalized composite spectrum for the entire sample is shown in red in Fig. 4; that adopted using Adelberger et al. (2003)’s velocity offset prescription is shown in black. The most striking difference is found around the $\text{Ly}\alpha$ emission. The red spectrum presents a prominent, asymmetric line. On the other hand, the black shows a less peaked signal with a broad tail to the blue side of the emission. This originates from the simple linear relation of Adelberger et al. (2003), $\Delta v_{\text{Ly}\alpha} \simeq 670 - 8.9\text{EW}$, whereby a fraction of the VIMOS LAEs with $\text{EW} \gtrsim 75 \text{ \AA}$ would be predicted to have a blueshifted $\text{Ly}\alpha$ emission with respect to the systemic redshift. We can also evaluate the validity of the composite method by measuring the EWs of $\text{Ly}\alpha$. We determine the $\text{EW}(\text{Ly}\alpha)$ from the black and red spectrum as $31 \pm 8 \text{ \AA}$ and $67 \pm 17 \text{ \AA}$, respectively. Given the typical $\text{EW}(\text{Ly}\alpha)$ of 73 \AA estimated from the narrow-band photometry in the VIMOS-LAEs sample, we consider the red spectrum using equation (1) to be the more accurate prescription. Additionally, the sought-after diagnostic UV lines of C III] , C IV , and O III] are detected with greater significance in the red composite spectrum, whilst the noise level around these emission lines is greater in the black spectrum. Fig. 4 thus demonstrates that the prescription of

equation (1) is preferred for the $\Delta v_{\text{Ly}\alpha}$ estimation from $\text{EW}(\text{Ly}\alpha)$, especially for LAEs with a large EW.

To evaluate sample variance and statistical noise, we adopt a bootstrap technique, similar to that used in Shapley et al. (2003). We generated 1000 fake composite spectra constructed from the sample of spectra used in creating the real composite spectra. Each fake spectrum was constructed in the same way, with the same number of spectra as the actual composite, but with the list of input spectra formulated by selecting spectra at random, with replacement, from the full list of VIMOS LAE spectra. With these 1000 fake spectra, we derived the standard deviation at each dispersion pixel. The standard deviations are taken into account in the following analyses based on line fluxes and EWs.

3.2.1 Dependencies

To examine spectroscopic trends in the LAE sample, we now split the data set into various subsamples based on the properties of the individual spectra. Since most of the LAEs are faint, we simply divide the sample into two halves to maximize the S/N of the resulting composite spectra. We chose the key properties of the $\text{EW}(\text{Ly}\alpha)$, absolute UV magnitude M_{UV} , and UV continuum slope β to investigate the various trends. The median and the threshold values are $\text{EW}(\text{Ly}\alpha) = 73 \text{ \AA}$, $M_{\text{UV}} = -19.5$, and $\beta = -1.50$. Note that the subsamples selected according to the UV slope are somewhat smaller since some LAEs lack the necessary multiple bands of rest-frame photometry. The composite spectra of the subsamples are shown in Fig. 5, and the various properties derived from the composite spectra are listed in Table 4. The errors on these entries take into account the variance measure on the stacked spectra as detailed above.

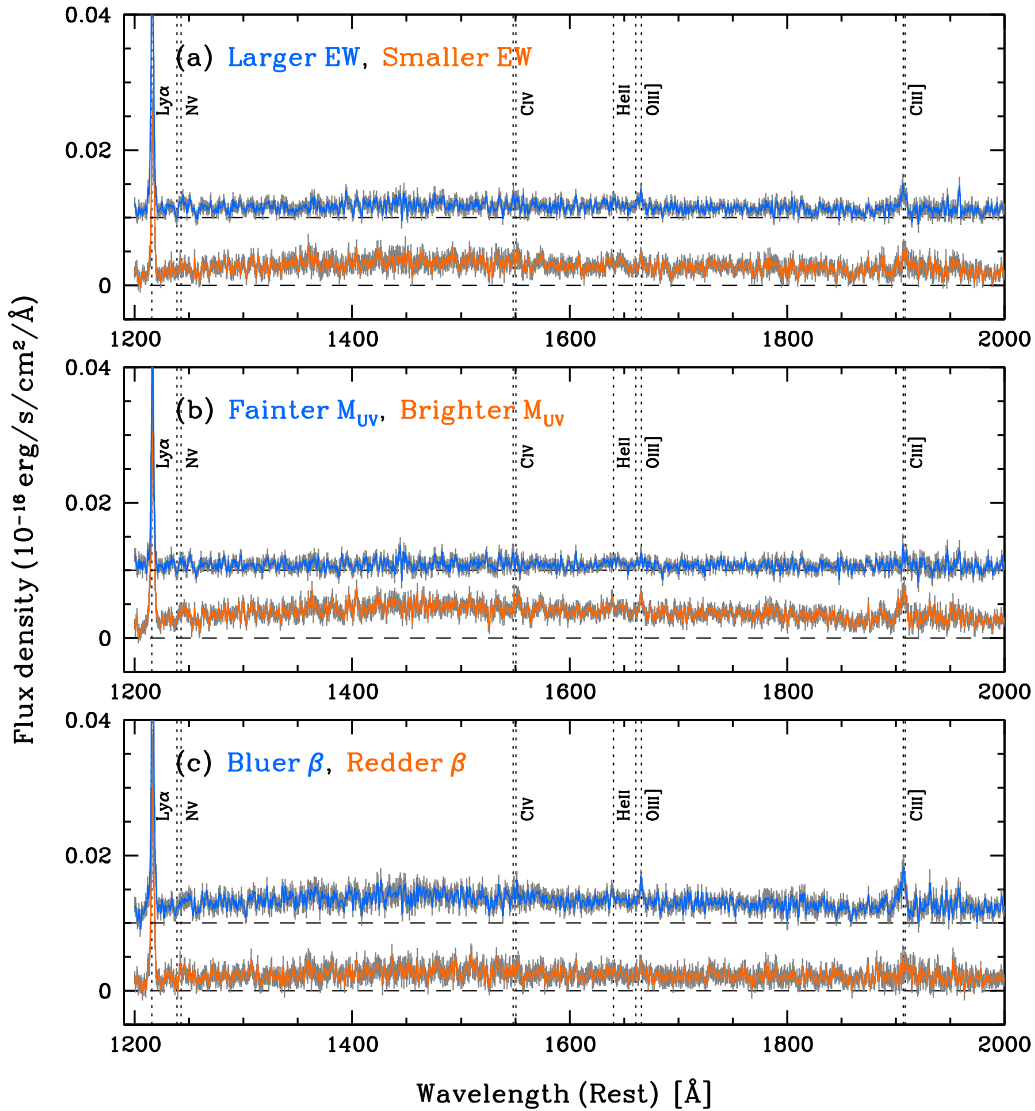


Figure 5. Composite rest-frame spectra of the VIMOS LAEs separated according to the strength of (a) EW(Ly α), (b) M_{UV} , and (c) UV slope β . In each case, the smaller/fainter and larger/brighter subsamples are displayed in blue/orange, respectively, in each panel. For convenience, the blue spectrum is offset vertically. The grey shaded region around each spectrum refers to the standard deviation of the flux density at each wavelength estimated by bootstrap resampling (see the text for details). The wavelengths of key diagnostic emission lines are marked with a dotted line.

Table 4. Spectroscopic properties of subsamples.

	Smaller EW(Ly α)	Larger EW(Ly α)	Brighter M_{UV}	Fainter M_{UV}	Redder β	Bluer β
N_{gal}	35	35	35	35	25	26
$\langle EW(Ly\alpha) \rangle$	38.	119.	40.	113.	42.	63.
$\langle M_{UV} \rangle$	-20.00	-19.20	-20.32	-18.97	-19.72	-19.69
$\langle \beta \rangle$	-1.5	-2.3	-1.5	-3.3	-1.2	-2.0
CIV EW	1.41 ± 0.53	2.91 ± 0.77	1.75 ± 0.45	3.88 ± 1.18	< 1.57	1.61 ± 0.47
CIV/CIII]	0.36 ± 0.16	0.29 ± 0.09	0.30 ± 0.08	0.49 ± 0.19	< 0.39	0.22 ± 0.07
CIV/CIII] _{corr} ^(†)	0.46 ± 0.20	0.32 ± 0.09	0.38 ± 0.11	0.49 ± 0.19	< 0.54	0.25 ± 0.08
HeII EW	1.15 ± 0.35	1.83 ± 0.45	1.26 ± 0.30	2.03 ± 0.53	1.12 ± 0.34	1.52 ± 0.38
HeII EW _{corr} ^(‡)	0.15 ± 0.05	0.83 ± 0.26	0.26 ± 0.08	1.03 ± 0.34	0.11 ± 0.04	0.51 ± 0.17
HeII/CIII]	0.26 ± 0.10	0.19 ± 0.05	0.20 ± 0.05	0.26 ± 0.09	0.22 ± 0.09	0.19 ± 0.05
HeII/CIII] _{corr} ^{(†)(‡)}	0.039 ± 0.020	0.089 ± 0.038	0.050 ± 0.020	0.130 ± 0.062	0.029 ± 0.016	0.073 ± 0.031
O III] EW	1.89 ± 0.66	4.67 ± 0.87	1.99 ± 0.30	3.60 ± 1.32	1.68 ± 0.41	2.95 ± 0.36
O III]/CIII]	0.42 ± 0.17	0.45 ± 0.10	0.31 ± 0.06	0.39 ± 0.17	0.34 ± 0.12	0.37 ± 0.07
O III]/CIII] _{corr} ^(†)	0.49 ± 0.20	0.47 ± 0.11	0.36 ± 0.07	0.39 ± 0.17	0.41 ± 0.15	0.41 ± 0.07
CIII] EW	5.41 ± 1.20	15.14 ± 1.99	9.17 ± 0.98	11.05 ± 2.62	5.89 ± 1.57	10.99 ± 1.41

Notes. (†) Corrected for reddening. (‡) Corrected for the HeII stellar emission (Section 3.2.2).

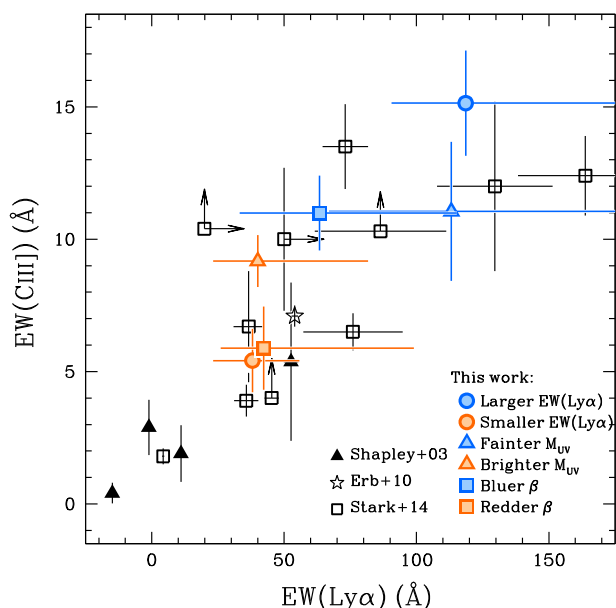


Figure 6. Relationship between $EW(\text{Ly}\alpha)$ and $EW(\text{CIII])}$ for the VIMOS and other samples. The blue and orange filled symbols show the composites of the six VIMOS subsamples as indicated in the legend. The black symbols refer to measures for $z = 2-3$ galaxies compiled from the literature as described in the legend.

We begin by discussing Fig. 6 which presents the correlation between $EW(\text{Ly}\alpha)$ and $EW(\text{CIII])}$ for the subsamples. A clear trend is obvious and follows that previously reported (Stark et al. 2014; Rigby et al. 2015; Le Fèvre et al. 2017). CIII] emission is stronger in LAEs with larger $EW(\text{Ly}\alpha)$, fainter M_{UV} , and bluer UV slopes. Similar trends are also observed in CIV , OIII] , and HeII emission (corrected; Section 3.2.2). As clarified by earlier studies with photoionization models (Jaskot & Ravindranath 2016; Nakajima et al. 2017), simple stellar populations find it hard to reproduce CIII] with $EW \gtrsim 10 \text{ \AA}$ and populations including the contribution of massive binary systems have been proposed (Section 4).

3.2.2 Corrections to the nebular spectra

To ensure the intrinsic nebular spectra of the VIMOS LAEs can be directly compared with photoionization models (Section 3.3), we must apply several corrections to the observed UV spectra.

First, we need to correct for the contribution of stellar emission. The HeII emission line is a composite of both stellar and nebular emission (e.g. Brinchmann, Pettini & Charlot 2008; Erb et al. 2010; Steidel et al. 2016). Since our VIMOS data do not have the spectral resolution necessary to resolve the two components, we use a stellar synthesis code to predict the stellar contribution and hence subtract it. We use publicly available *BPASS* (v2.0; Stanway, Eldridge & Becker 2015) SEDs including binary evolution to predict the stellar HeII emission strengths. Considering a current star formation age of 10 to several 100 Myr as plausible for LAEs (e.g. Gawiser et al. 2006, 2007; Ono et al. 2010; Kusakabe et al. 2018), the stellar HeII emission is predicted to have $EW \simeq 0.8-1.4 \text{ \AA}$.²

² The stellar HeII emission strength is estimated to be $EW \simeq 0.8-1.2 \text{ \AA}$ if we adopt the v2.1 *BPASS* models (Eldridge et al. 2017). Our results are thus not affected by the choice between v2.0 and v2.1. In this paper, we use the v2.0 *BPASS* models, which are also adopted in the photoionisation models of Nakajima et al. (2017) (Section 3.3).

As a fiducial value, we adopt a value of $1.0 \pm 0.2 \text{ \AA}$, as used by Nakajima et al. (2017). We consider this appropriate for a sub-solar metallicity of $Z \simeq 0.2-0.5 Z_{\odot}$ (e.g. Nakajima et al. 2013; Trainor et al. 2016). If a lower metallicity were assumed, the stellar HeII emission could be slightly larger, $1.2 \pm 0.2 \text{ \AA}$.

A further correction is required for dust reddening. In Paper I, we assumed such a correction is negligible for LAE. Here, in an improvement, we utilize the UV slope β obtained from the Subaru photometry in conjunction with our stellar population models. Using the SMC extinction curve and the *BPASS* SEDs (Reddy et al. 2018), we correct for the reddening of the line ratios for each of the six subsamples using the median value of β . The corrections are small and do not affect our results significantly. As an example, for the subsample with weaker $EW(\text{Ly}\alpha)$ $\beta \simeq 1.5$ and the corrected $\text{CIV}/\text{CIII]}$ ratio (which spans the widest wavelength range we use) is increased by a factor of ~ 1.3 , which is within the 1σ uncertainties. Although it is debatable whether nebular emission and the stellar continuum suffer the same amount of dust attenuation (e.g. Reddy et al. 2015), such differences will not be a concern for measures based on EWs.

3.3 UV diagnostic diagrams

Following the corrections adopted in Section 3.2.2, we now proceed to interpret the UV spectra of our various VIMOS subsamples using three UV diagnostic emission line ratios in Fig. 7. Since these are high ionization lines, UV line diagnostics such as CIII] , CIV and HeII were initially applied to spectra of radio galaxies and AGNs (e.g. Villar-Martín, Tadhunter & Clark 1997; Allen, Dopita & Tsvetanov 1998; Groves, Dopita & Sutherland 2004; Nagao, Maiolino & Marconi 2006; Dors et al. 2014). There is now broader interest in studying these lines to gauge the ionization field in star-forming galaxies, both theoretically (e.g. Feltre et al. 2016; Gutkin et al. 2016; Nakajima et al. 2017) and observationally (e.g. Stark et al. 2014; Amorín et al. 2017; Le Fèvre et al. 2017). Our goal is to derive the physical properties of the gaseous phase in the interstellar medium (ISM) in the context of the hardness of the ionizing spectrum, as characterized by ξ_{ion} – the number of LyC photons per UV luminosity.

In the following, we follow the procedures introduced by Nakajima et al. (2017). In that work UV diagnostic diagrams are interpreted with photoionization models which include incident radiation fields of both stellar populations and AGN and cover a wide range of metallicities and ionization parameters. The authors demonstrate how such diagrams can be used not only to separate star-forming galaxies from AGN but also to constrain ξ_{ion} for star-forming galaxies. Fortunately, as expected, Fig. 7 demonstrates that all of our various LAE subsamples are consistent with star-forming regions. Thus, in the following, we use only the stellar photoionization models to discuss their properties. We briefly describe the details of the stellar photoionization models below.

Our stellar photoionization models are based on *CLOUDY* (version 13.03; Ferland et al. 1998, 2013) and assume constant density homogeneous inter-stellar gas with a plane-parallel geometry. Dust physics and elemental depletion factors follow the analyses of Dopita et al. (2006) and Nagao et al. (2011). All elements except nitrogen, carbon and helium are taken to be primary nucleosynthesis elements. For carbon and nitrogen, we use the formalism of Dopita et al. (2006) and López-Sánchez et al. (2012), respectively, to account for their secondary products. For helium, we adopt the form given by Dopita et al. (2006). The photoionization models are

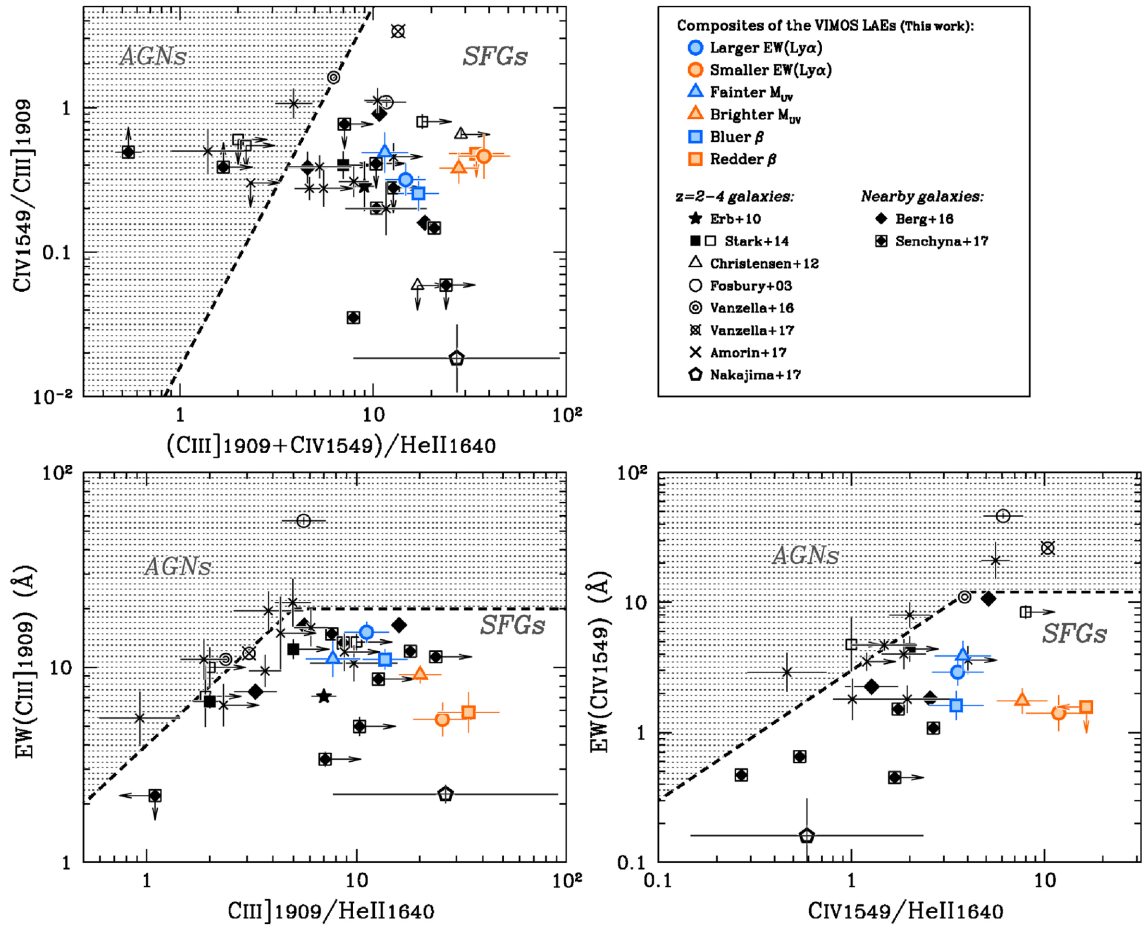


Figure 7. Diagnostic diagrams involving various UV emission line ratios: $CIV/CIII]$ versus $(CIII]+CIV)/HeII$ (top left-hand panel), $EW(CIII])$ versus $CIII]/HeII$ (bottom left-hand panel), and $EW(CIV)$ versus $CIV/HeII$ (bottom right-hand panel). Blue and orange symbols present the six VIMOS subsamples as shown in the legend. The black symbols are $z = 0-4$ star-forming galaxies compiled from the literature by Nakajima et al. (2017), as shown in the legend. In these diagrams, star-forming galaxies can be separated from AGNs, which are dominated in the grey hatched areas (see Nakajima et al. 2017).

calculated by varying the metallicity and ionization parameter, fixing the gas density $n_H = 10^2 \text{ cm}^{-3}$. For the radiation field, we adopt the population synthesis code `BPASS` (v2.0; Stanway et al. 2015) for binary star populations and `POPSTAR` (Mollá, García-Vargas & Bressan 2009) for single stellar populations. Stellar metallicities are matched to their gas-phase equivalents. We assume a constant star formation history and vary the duration of current star formation from 1 to 1000 Myr. An older age corresponds to a lower ξ_{ion} parameter. Emission line ratios are insensitive to the duration of star formation, but the EWs of UV lines are affected as the continuum level strongly depends on the older stellar population. The advantage of using the models of Nakajima et al. (2017) is that they predict EWs of the UV lines as a function of metallicity, ionization parameter, and ξ_{ion} .

We evaluate the average ionization parameter and metallicity by fitting stellar photoionization models to the most sensitive line ratios of $CIV/CIII]$ and $(CIII]+CIV)/HeII$. The estimation procedure is similar to that typically adopted for the optical $[OIII]/[OII] - ([OII]+[OIII])/H\beta$ diagram (e.g. Kewley & Dopita 2002; Kobulnicky & Kewley 2004; Nakajima & Ouchi 2014) but here applied to more highly ionized nebular regions. The $(CIII]+CIV)/HeII$ is sensitive to metallicity and increases towards a higher metallicity. This is because of (i) an increase of carbon element and (ii) a

softening of the radiation field (i.e. a weakening of the $HeII$ emission) with increasing metallicity. The $CIV/CIII]$ is mainly governed by the ionization parameter and increases with it. Moreover, the $(CIII]+CIV)/HeII$ ($CIV/CIII]$) ratio also has a weak dependency on the ionization parameter (metallicity). We therefore use both the ratios of $(CIII]+CIV)/HeII$ and $CIV/CIII]$ to estimate the metallicity and ionization parameter simultaneously. The top left-hand panel of Fig. 7 shows that LAEs with larger $EW(Ly\alpha)$, fainter M_{UV} , and bluer UV slopes (hereafter called the ‘stronger LAEs sample’) tend to present a smaller $(CIII]+CIV)/HeII$ ratio. This indicates that the stronger LAEs sample has a lower gas-phase metallicity – a result that would not be affected if we adopted a stronger correction for stellar emission of $EW(HeII)_{stellar} = 1.2 \pm 0.2 \text{ \AA}$ (Section 3.2.2). Based on the binary stellar population photoionization models, the stronger LAEs sample has an average metallicity of $Z \simeq 0.05-0.2 Z_{\odot}$, while the weaker LAEs sample has a somewhat higher metallicity of $Z \simeq 0.1-0.5 Z_{\odot}$. The ionization parameters U – defined as the ratio of the ionizing photon flux to the gas density – are constrained at the same time, differ with $\log U \simeq -1.5$ to -2.2 for the stronger LAEs sample compared to $\log U \simeq -2.0$ to -2.5 for the weaker LAEs sample. We derive the best fit and 1σ uncertainty of metallicity and ionization parameter for each of the three sub-samples in the stronger and weaker LAEs samples. The ranges

Table 5. Summary of the inferred properties of the VIMOS LAEs with the UV lines.

Sample	Input radiation	$Z (Z_{\odot})$	$\log U$	Age (Myr)	$\log \xi_{\text{ion}}/\text{erg}^{-1} \text{ Hz}$
Stronger LAEs	<i>(Subsamples of larger EW(Lyα), fainter M_{UV}, bluer UV slope)</i>				
	binary stellar pop.	0.05 ... 0.2	-2.2 ... -1.5	$\lesssim 20$	25.68 ± 0.13
Weaker LAEs	<i>(Subsamples of smaller EW(Lyα), brighter M_{UV}, redder UV slope)</i>				
	binary stellar pop.	0.1 ... 0.5	-2.5 ... -2.	10 ... 500	25.54 ± 0.09

of the properties above are given to cover the properties of the three sub-samples including the 1σ uncertainties. Although the subsample of LAEs with the redder UV slope does not exhibit a significant C_{IV} detection, its relatively large EW(C_{III}) ensures that its ionization parameter could not be less than $\log U \simeq -2.5$. These quantities are not significantly altered if we adopt the single stellar population models.

One uncertainty in the analysis is the use of C_{IV} as a diagnostic tool. Since C_{IV} line photons can be trapped in a highly ionized nebular region by resonant scattering, they would be preferentially absorbed and weakened by internal dust. Although dust physics is included in the modelling, there remain uncertainties in accurately modelling how this affects C_{IV} emission. For this work, we find that the LAEs are on average fairly free from dust with $E(B - V) = 0.09 \pm 0.07$ (Section 2.1) and so assume C_{IV} measures will not be severely affected.

It is important to note that these models also reproduce our O_{III}] emission line strengths. Since the stellar photoionization models of Nakajima et al. (2017) by default assume an empirical relationship between C/O and O/H ratios (Dopita et al. 2006) to give a carbon abundance at each metallicity, LAEs are on average expected to obey the same relationship, as typically inferred for continuum-selected galaxies at similar redshifts (e.g. Steidel et al. 2016). Using the method of Pérez-Montero & Amorín (2017), the C/O ratios are estimated from the (C_{III}+C_{IV})/O_{III}] ratios to be $\log C/O \simeq -0.7 \pm 0.1$.

3.4 The hardness of the ionizing spectrum

Finally, with the knowledge of the metallicity and ionization parameter U , we turn to estimating the hardness of the ionizing spectrum, ξ_{ion} . We consider both the EW(C_{III}) and EW(C_{IV}) diagnostic diagrams presented in the two lower panels of Fig. 7.

The strength of the various UV lines is sensitive not only to the ISM condition but also to the ratio of the number of ionizing photons to the (non-ionizing) UV continuum, i.e. ξ_{ion} . The UV nebular continuum must also be considered for an accurate analysis. Using the derived ISM properties (Section 3.3) and assuming a constant star formation rate, we vary the duration of current star formation from 1 to 1000 Myr in order to match the observed EWs of C_{III}] and C_{IV}. The inferred age can then be directly translated into a constraint on ξ_{ion} . It is important to note that in the following derivation of ξ_{ion} we will follow the convention of assuming a zero escape fraction of ionizing photons (see discussion in Section 4).

The derivation of ξ_{ion} also depends on whether or not the stellar population includes binary stars. As clarified by Nakajima et al. (2017), EWs of C_{III}] and C_{IV} generated by a single stellar population produce $\text{EW}(\text{C}_{\text{III}}] \lesssim 12 \text{ \AA}$ and $\text{EW}(\text{C}_{\text{IV}}) \lesssim 9 \text{ \AA}$, whereas binary stellar populations yield EWs as large as ~ 20 and $\sim 12 \text{ \AA}$, respectively (see also Jaskot & Ravindranath 2016). Since the stronger LAEs sample shows EW(C_{III}]s of $\simeq 13 \text{ \AA}$, a single stellar population is

likely insufficient. We therefore adopt the binary stellar population models for the stronger LAEs sample.

After some consideration, we decided to focus on using the EW(C_{III}] figure (lower left-hand panel in Fig. 7) to estimate ξ_{ion} . There remains a concern that the C_{IV} measurements may be affected by underlying stellar absorption. For the stronger LAEs sample, the large EW(C_{III}] is consistent with a young star formation age and a high ξ_{ion} . The inferred age spans a few Myr in the lowest metallicity case ($Z \simeq 0.05 Z_{\odot}$) to ~ 20 Myr at $Z \simeq 0.2 Z_{\odot}$. The resulting average value of ξ_{ion} is then $\log \xi_{\text{ion}}/\text{erg}^{-1} \text{ Hz} \simeq 25.68 \pm 0.13$. This error includes the uncertainties of the EW(C_{III}]s as well as those of the inferred ISM properties (Section 3.3). Likewise, the weaker LAEs sample is diagnosed to have a current star formation age of ~ 10 to 500 Myr and $\log \xi_{\text{ion}}/\text{erg}^{-1} \text{ Hz} \simeq 25.54 \pm 0.09$ if the binary stellar population models are assumed. The difference between the two samples arises primarily from the different C_{III}] EWs.

One uncertainty in interpreting ξ_{ion} for the weaker LAEs sample is whether or not to include binary stars in the stellar population. If we adopt the single star models, the star formation age is significantly reduced to ~ 1 –7 Myr with $\log \xi_{\text{ion}}/\text{erg}^{-1} \text{ Hz} \simeq 25.5$ –25.7. The younger age arises from the fact that (i) single star models predict a smaller maximum EW of C_{III}], and (ii) EW(C_{III}] weakens more rapidly whereas binary evolution prolongs the period during which blue stars dominate the spectrum (see also Nakajima et al. 2017). It is unlikely, however, that the weaker LAEs population is so young (cf. Gawiser et al. 2006, 2007; Ono et al. 2010; Guaita et al. 2011; Kusakabe et al. 2018) and indeed even younger than the stronger LAEs population. We note that typical ages inferred for the LBG population at similar redshifts are several $\times 100$ Myr (e.g. Reddy et al. 2012; Nakajima et al. 2017) where binary star models are preferred. Since the weaker LAEs can logically be considered to represent a population intermediate between LBGs and the stronger LAEs (e.g. Steidel et al. 2016; Trainor et al. 2016; Nakajima et al. 2017), it seems reasonable to include binary stars.

The ISM properties and ξ_{ion} derived from the comparison of the UV emission lines with the photoionization models of Nakajima et al. (2017) are given in Table 5. The uncertainties on ξ_{ion} reflect both the variance arising from the use of stacked spectra and the range of ages considered.

4 DISCUSSION

We present VIMOS measurements of the rest-frame UV nebular emission lines of C_{III}], C_{IV}, HeII, and O_{III}] drawn from a sample of $70 z = 3.1$ LAEs. By dividing the sample into nearly equal subsets based on the EW(Ly α), UV magnitude M_{UV} , and UV slope β , we demonstrate that the ‘stronger LAEs sample’ with larger EW(Ly α), fainter M_{UV} and bluer β have stronger EWs of C_{III}] emission and smaller (C_{III}+C_{IV})/HeII line ratios than the corresponding ‘weaker LAEs sample’.

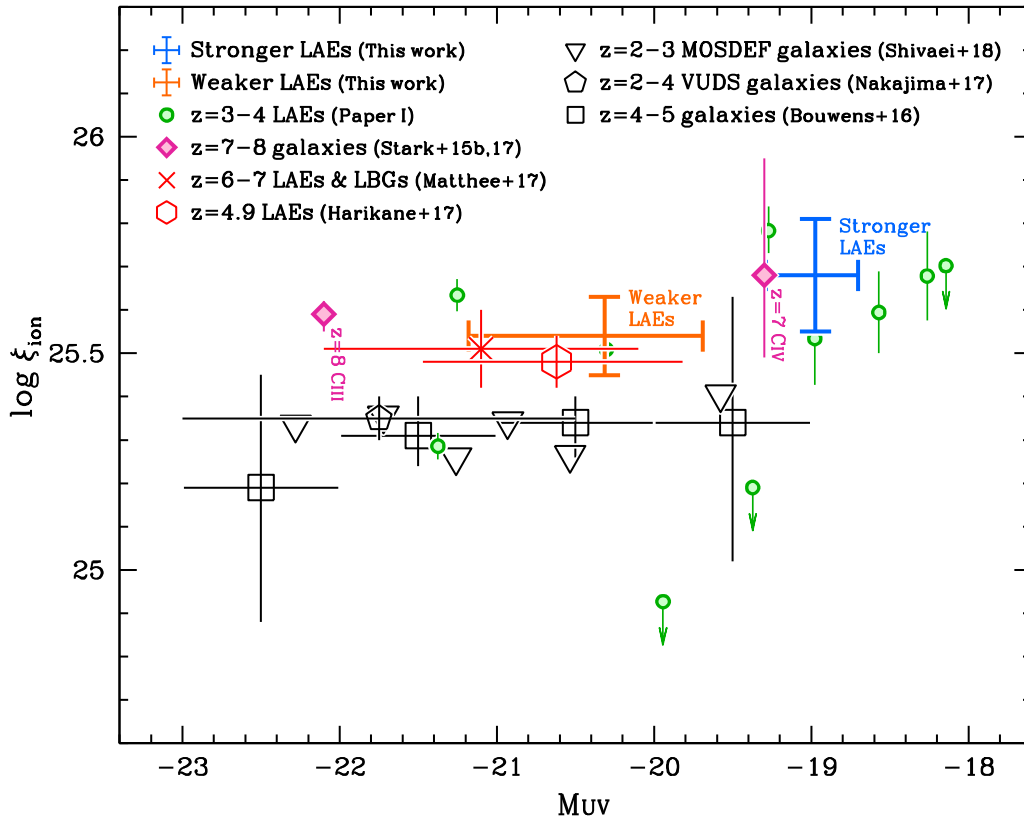


Figure 8. The efficiency of ionizing photon production ξ_{ion} as a function of UV absolute magnitude. Blue and orange refer to the stronger and the weaker LAEs samples, respectively. Green circles are individual LAEs whose ξ_{ion} were derived from $H\beta$ measures and recombination theory (Paper I). Among the 13 LAEs presented in Paper I, one AGN-LAE and two LAEs whose ξ_{ion} is less reliable are not displayed. Magenta diamonds present a $z = 7.05$ galaxy identified with C IV (Stark et al. 2015b) and a $z = 7.73$ galaxy identified with C $\text{III]$ (Stark et al. 2017). Red crosses represents a compilation of $z = 6-7$ luminous Ly α -selected and UV-selected galaxies (Matthee et al. 2017), and the red hexagon is an average for LAEs at $z = 4.9$ (Harikane et al. 2017). Black open symbols show larger samples of continuum-selected LBGs at similar redshifts; from MOSDEF (inverse triangles; Shivaeei et al. 2018; at $z = 1.4-2.6$), VUDS (pentagon; Nakajima et al. 2017; at $z = 2-4$; see also Le Fèvre et al. 2015, 2017), and Bouwens et al. (2016) (squares; at $z = 3.8-5.0$). An SMC attenuation law is adopted in the correction for dust reddening. ξ_{ion} values are calculated under the assumption of a zero escape fraction of ionizing photons excepting for those from MOSDEF, which refer to an assumed value of 9 percent (see the text for details).

Using our photoionization models and the UV diagnostic diagrams presented in Nakajima et al. (2017), we interpret these trends as indicating that the stronger LAEs sample, which represents the more intense LAE phenomenon, has typically a lower gas phase metallicity and, importantly, a more efficient production of ionizing photons. In addition to inferring a higher ξ_{ion} , binary stars are essential in our modelling to reproduce the EWs of C $\text{III]$.

We can place our results in context by examining, in Fig. 8, the distribution of ξ_{ion} as a function of M_{UV} for the two subsamples of the VIMOS LAEs as well as for other high redshift sources, including the modest sample of LAEs studied with MOSFIRE in Paper I for which ξ_{ion} was inferred from $H\beta$ using recombination theory. We also include various $z \simeq 5-8$ galaxies (Stark et al. 2015b, 2017; Harikane et al. 2017; Matthee et al. 2017) for comparison purposes including several exploiting C $\text{III]$ emission, and continuum-selected LBGs at $z = 2-5$ (Bouwens et al. 2016; Nakajima et al. 2017; Shivaeei et al. 2018). The ξ_{ion} parameters of Stark et al. (2015b, 2017) and Nakajima et al. (2017) are based on the UV emission lines with photoionization models as we adopt in this paper, while the other studies estimate ξ_{ion} from hydrogen recombination lines.

Over the UV magnitude range from $M_{\text{UV}} \simeq -19.5$ to -22.5 , the continuum-selected LBGs at $z = 2-5$ show a uniform value, $\log \xi_{\text{ion}}/\text{erg}^{-1} \text{Hz} \simeq 25.2-25.4$. On the other hand, LAEs have a

consistently larger value by $\sim 0.2-0.3$ dex, as originally claimed from a much smaller sample in Paper I. Our analysis has also shown that UV faint LAEs present a higher ξ_{ion} than their luminous counterparts.

The most intriguing comparison is with the emerging data in the reionization era. Although the uncertainties remain large, and the samples modest in size, the large values of ξ_{ion} inferred for the faintest metal-poor VIMOS LAEs are similar to those observed in galaxies at $z > 6$ (Stark et al. 2015b, 2017; Matthee et al. 2017; Harikane et al. 2017). Since our LAEs likewise present intense [O $\text{III]}\lambda\lambda 5007, 4959$ emission (Paper I) as inferred indirectly from *Spitzer*/IRAC photometry for $z > 6$ star-forming galaxies (Smit et al. 2014, 2015; Oesch et al. 2015; Roberts-Borsani et al. 2016; Harikane et al. 2017), we conclude they remain valuable low-redshift analogues of the possible sources of cosmic reionization.

In order to understand the physical origin of the intense C $\text{III]$ and Ly α emission, which combine to define the ‘stronger LAE sample’ as illustrated in Fig. 6, we present in Fig. 9 the distribution of EW(C $\text{III]})$ as a function of metallicity. Here, we compare data from our two VIMOS-LAEs sub-samples with other relevant galaxies compiled from the literature.

It is clear from Fig. 9 that galaxies with a lower metallicity present a larger EW C III] . One reason is that C III] EW peaks at

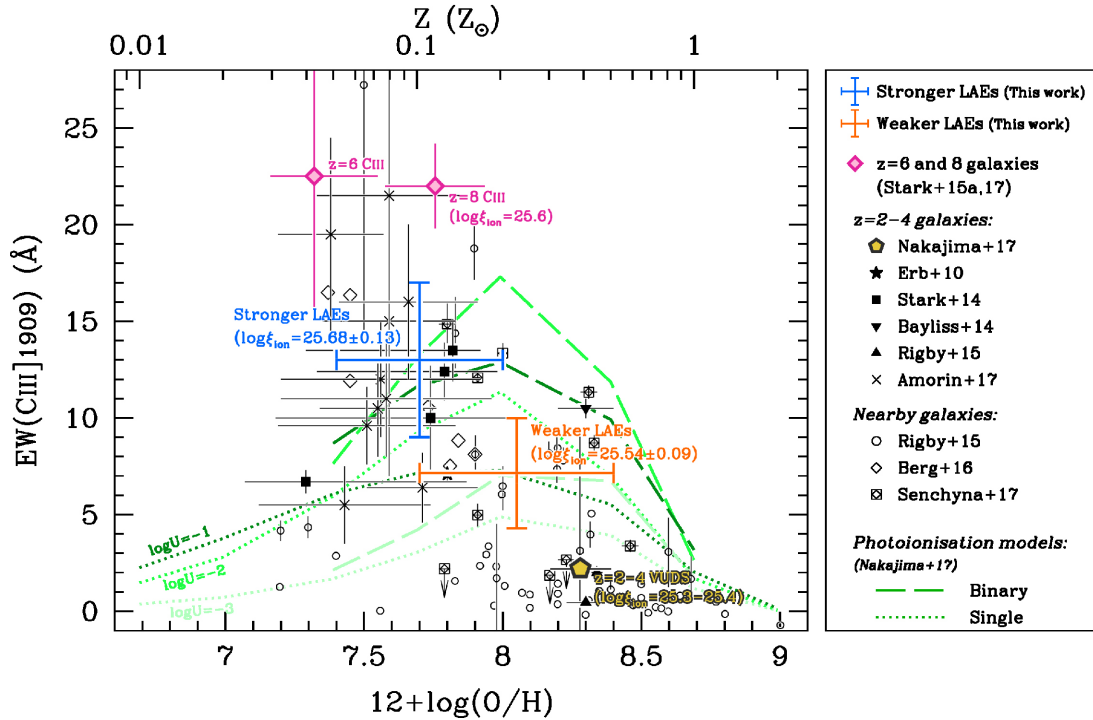


Figure 9. The $\text{EW}(\text{C III]})$ as a function of metallicity. The stronger and weaker LAEs sample are indicated by the blue and orange error bars, respectively. The magenta symbol present the $z = 7.73$ galaxy identified with C III] (Stark et al. 2017), and the black symbols represent $z = 0-4$ galaxies compiled from the literature as shown in the legend. The average LBG population at $z = 2-4$ drawn from VUDS (Nakajima et al. 2017) for which a ξ_{ion} measurement is available is highlighted in yellow. Green curves present photoionization models using single- (dotted) and binary- (long dashed) stellar populations (Nakajima et al. 2017) and trace the maximum EW for a given metallicity and a range of ionization parameters: $\log U = -1$ (dark green), -2 (green), and -3 (light green).

sub-solar metallicities, as shown with the photoionization models. Another arises because the ionization parameter becomes higher at lower metallicity. $\text{EW}(\text{C III]})$ increases with ionization parameter for a given metallicity up to $\log U \simeq -2$. As emphasized earlier, binary stellar populations can also produce stronger EWs of C III] than single stellar populations at a fixed ISM properties (Nakajima et al. 2017), although it seems likely binary stellar populations are an ubiquitous feature of early star-forming galaxies.

The other important parameter governing the $\text{EW}(\text{C III]})$ is ξ_{ion} , or the age of the current star formation. The photoionization models in Fig. 9 are based on 1 Myr old stellar populations providing a maximal $\text{EW}(\text{C III]})$ for a given ISM condition. Weaker EWs correspond to longer star formation ages and lower ξ_{ion} .

Finally, we issue some caveats. The most important variable that could change our ξ_{ion} estimates is the escape fraction of ionizing photons. EWs of C III] and C IV would be weakened with a higher escape fraction for a fixed ISM condition, since less ionizing photons are necessary to produce the high ionization lines (see also Jaskot & Ravindranath 2016). For example, based on the models of Jaskot & Ravindranath (2016), for galaxies with a sub-solar metallicity, an ionization parameter of $\log U \simeq -2.5$, and a 20 per cent escape fraction would lower the EW of C III] by a factor of $\lesssim 1.3$ as compared with the zero escape fraction case. However, in the specific case of the MOSDEF survey of LBGs (Shivaei et al. 2018) where an escape fraction of 9 per cent was typically assumed, applying a correction to our adopted value of zero would only raise those points by $\simeq 0.04$ dex in Fig. 8 and not change our conclusions. Inevitably until we can independently examine the LyC leakage from our sample, we cannot quantitatively break this degeneracy and determine an absolute ξ_{ion} .

A further issue is the fact our photoionization models predict that the C III] EW decreases if the metallicity becomes very much lower due to the lack of carbon. Presumably, the positive correlation between EWs of $\text{Ly}\alpha$ and C III] as shown in Fig. 6 indicates such systems have not yet been detected (see also Harikane et al. 2017; Nakajima et al. 2017).

Furthermore, the C/O abundance ratio could affect the interpretation. By default our photoionization models assume the empirical relationship between C/O and O/H ratios (Dopita et al. 2006) to predict the carbon lines strength. As discussed earlier, we have confirmed with $(\text{C III]} + \text{C IV})/\text{O III]}$ ratios that our VIMOS-LAEs typically have C/O ratios of $\log \text{C/O} \simeq -0.7 \pm 0.1$ and follow the empirical relation. However, this may not be true for higher- z galaxies. Indeed, the C III] -or- C IV emitting galaxies at $z = 7-8$ studied by Stark et al. (2015a,b, 2017) have best-fitting C/O ratios higher than expected from the empirical relation by $\sim 0.1-0.4$ dex. Although the constraints are very weak for these high- z objects with the limited data, their large EWs of C III] for their low metallicities, as presented in Fig. 9, would result from their elevated C/O ratios. The physical cause of such high C/O abundance ratios is unclear (see e.g. Mattsson 2010; Berg et al. 2016; Nakajima et al. 2017 for a discussion).

In summary, therefore, the more intense LAEs with strong C III] studied here and, by reference to Paper I, those with intense $[\text{O III}]$, can be considered to be young metal-poor galaxies in an early phase of galaxy evolution, providing a large amount of ionizing photons into the ISM to achieve highly ionized nebular regions. They remain excellent analogues of galaxies in the reionization era and, by virtue of their relative proximity and brightness, valuable targets for further detailed study.

ACKNOWLEDGEMENTS

We acknowledge financial support from European Research Council Advanced Grant FP7/669253 (TF, RSE). KN acknowledges a JSPS Overseas Research Fellowship. BER is supported in part by the program HST-GO-14747 provided by NASA through a grant from the Space Telescope Science Institute, which is operated by the Association of Universities for Research in Astronomy, Incorporated, under NASA contract NAS5-26555. It is a pleasure to thank Dan Stark, Masami Ouchi, Daniel Schaerer, and the anonymous referee for useful comments and discussions. We also thank T. Hayashino, T. Yamada, Y. Matsuda, and A. K. Inoue for providing the LAE catalogue and the photometric data. The work is based on data products from observations made with ESO Telescopes at the La Silla Paranal Observatory under ESO programme ID 098.A-0010(A). Further data was taken with the W.M. Keck Observatory on Maunakea, Hawaii which is operated as a scientific partnership among the California Institute of Technology, the University of California and the National Aeronautics and Space Administration. This Observatory was made possible by the generous financial support of the W. M. Keck Foundation. The authors wish to recognize and acknowledge the very significant cultural role and reverence that the summit of Maunakea has always had within the indigenous Hawaiian community. We are most fortunate to have the opportunity to conduct observations from this mountain.

REFERENCES

- Adelberger K. L., Steidel C. C., Shapley A. E., Pettini M., 2003, *ApJ*, 584, 45
- Allen M. G., Dopita M. A., Tsvetanov Z. I., 1998, *ApJ*, 493, 571
- Amorín R. et al., 2017, *NatAs*, 1, 0052
- Asplund M., Grevesse N., Sauval A. J., Scott P., 2009, *ARA&A*, 47, 481
- Berg D. A., Skillman E. D., Henry R. B. C., Erb D. K., Carigi L., 2016, *ApJ*, 827, 126
- Bouwens R. J., Smit R., Labbé I., Franx M., Caruana J., Oesch P., Stefanon M., Rasappu N., 2016, *ApJ*, 831, 176
- Brinchmann J., Pettini M., Charlot S., 2008, *MNRAS*, 385, 769
- Cassata P. et al., 2015, *A&A*, 573, A24
- Curtis-Lake E. et al., 2012, *MNRAS*, 422, 1425
- Dopita M. A. et al., 2006, *ApJS*, 167, 177
- Dors O. L., Jr, Cardaci M. V., Hägele G. F., Krabbe A. C., 2014, *MNRAS*, 443, 1291
- Eldridge J. J., Stanway E. R., Xiao L., McClelland L. A. S., Taylor G., Ng M., Greis S. M. L., Bray J. C., 2017, *PASA*, 34, 58
- Erb D. K., Pettini M., Shapley A. E., Steidel C. C., Law D. R., Reddy N. A., 2010, *ApJ*, 719, 1168
- Erb D. K. et al., 2014, *ApJ*, 795, 33
- Erb D. K., Pettini M., Steidel C. C., Strom A. L., Rudie G. C., Trainor R. F., Shapley A. E., Reddy N. A., 2016, *ApJ*, 830, 52
- Feltre A., Charlot S., Gutkin J., 2016, *MNRAS*, 456, 3354
- Ferland G. J., Korista K. T., Verner D. A., Ferguson J. W., Kingdon J. B., Verner E. M., 1998, *PASP*, 110, 761
- Ferland G. J. et al., 2013, *Rev. Mex. Astron. Astrofis.*, 49, 137
- Gawiser E. et al., 2006, *ApJ*, 642, L13
- Gawiser E. et al., 2007, *ApJ*, 671, 278
- Groves B. A., Dopita M. A., Sutherland R. S., 2004, *ApJS*, 153, 75
- Guaita L. et al., 2011, *ApJ*, 733, 114
- Gutkin J., Charlot S., Bruzual G., 2016, *MNRAS*, 462, 1757
- Harikane Y. et al., 2017, *ApJ*, preprint ([arXiv:1711.03735](https://arxiv.org/abs/1711.03735))
- Hashimoto T. et al., 2013, *ApJ*, 765, 70
- Hayashino T. et al., 2004, *AJ*, 128, 2073
- Inoue A. K., Iwata I., 2008, *MNRAS*, 387, 1681
- Inoue A. K., Shimizu I., Iwata I., Tanaka M., 2014, *MNRAS*, 442, 1805
- Iwata I. et al., 2009, *ApJ*, 692, 1287
- Izotov Y. I., Orlitová I., Schaerer D., Thuan T. X., Verhamme A., Guseva N. G., Worseck G., 2016a, *Nature*, 529, 178
- Izotov Y. I., Schaerer D., Thuan T. X., Worseck G., Guseva N. G., Orlitová I., Verhamme A., 2016b, *MNRAS*, 461, 3683
- Jaskot A. E., Ravindranath S., 2016, *ApJ*, 833, 136
- Kewley L. J., Dopita M. A., 2002, *ApJS*, 142, 35
- Kobulnicky H. A., Kewley L. J., 2004, *ApJ*, 617, 240
- Kusakabe H. et al., 2018, *PASJ*, 70, 4
- Le Fèvre O. et al., 2015, *A&A*, 576, A79
- Le Fèvre O. et al., 2017, *A&A*, preprint ([arXiv:1710.10715](https://arxiv.org/abs/1710.10715))
- Leitherer C., Hernandez S., Lee J. C., Oey M. S., 2016, *ApJ*, 823, 64
- López-Sánchez Á.R., Dopita M. A., Kewley L. J., Zahid H. J., Nicholls D. C., Scharwächter J., 2012, *MNRAS*, 426, 2630
- Madau P., 1995, *ApJ*, 441, 18
- Matsuda Y. et al., 2004, *AJ*, 128, 569
- Matsuda Y. et al., 2005, *ApJ*, 634, L125
- Matthee J. et al., 2017, *MNRAS*, 472, 772
- Mattsson L., 2010, *A&A*, 515, A68
- Meurer G. R., Heckman T. M., Lehnert M. D., Leitherer C., Lowenthal J., 1997, *AJ*, 114, 54
- Micheva G., Iwata I., Inoue A. K., Matsuda Y., Yamada T., Hayashino T., 2017, *MNRAS*, 465, 316
- Mollá M., García-Vargas M. L., Bressan A., 2009, *MNRAS*, 398, 451
- Momose R. et al., 2016, *MNRAS*, 457, 2318
- Nagao T., Maiolino R., Marconi A., 2006, *A&A*, 447, 863
- Nagao T., Maiolino R., Marconi A., Matsuhara H., 2011, *A&A*, 526, 149
- Nakajima K., Ouchi M., 2014, *MNRAS*, 442, 900
- Nakajima K., Ouchi M., Shimasaku K., Hashimoto T., Ono Y., Lee J. C., 2013, *ApJ*, 769, 3
- Nakajima K., Ellis R. S., Iwata I., Inoue A. K., Kusakabe H., Ouchi M., Robertson B. E., 2016, *ApJ*, 831, L9 (Paper I)
- Nakajima K. et al., 2017, *A&A*, preprint ([arXiv:1709.03990](https://arxiv.org/abs/1709.03990))
- Nestor D. B., Shapley A. E., Kornei K. A., Steidel C. C., Siana B., 2013, *ApJ*, 765, 47
- Nilsson K. K. et al., 2009, *A&A*, 498, 13
- Nilsson K. K. et al., 2011, *A&A*, 529, A9
- Oesch P. A. et al., 2015, *ApJ*, 804, L30
- Ono Y. et al., 2010, *MNRAS*, 402, 1580
- Pérez-Montero E., Amorín R., 2017, *MNRAS*, 467, 1287
- Reddy N. A. et al., 2012, *ApJ*, 754, 25
- Reddy N. A. et al., 2015, *ApJ*, 806, 259
- Reddy N. A. et al., 2018, *ApJ*, 853, 56
- Rigby J. R. et al., 2015, *ApJ*, 814, L6
- Roberts-Borsani G. W. et al., 2016, *ApJ*, 823, 143
- Robertson B. E. et al., 2013, *ApJ*, 768, 71
- Schaerer D., Izotov Y. I., Verhamme A., Orlitová I., Thuan T. X., Worseck G., Guseva N. G., 2016, *A&A*, 591, L8
- Schenker M. A., Ellis R. S., Konidaris N. P., Stark D. P., 2013, *ApJ*, 777, 67
- Schlegel D. J., Finkbeiner D. P., Davis M., 1998, *ApJ*, 500, 525
- Shapley A. E., Steidel C. C., Pettini M., Adelberger K. L., 2003, *ApJ*, 588, 65
- Shibuya T. et al., 2014, *ApJ*, 788, 74
- Shivaei I. et al., 2018, *ApJ*, 855, 42
- Smit R. et al., 2014, *ApJ*, 784, 58
- Smit R. et al., 2015, *ApJ*, 801, 122
- Song M. et al., 2014, *ApJ*, 791, 3
- Stanway E. R., Eldridge J. J., Becker G. D., 2015, *MNRAS*, 456, 485
- Stark D. P., Ellis R. S., Ouchi M., 2011, *ApJ*, 728, L2
- Stark D. P. et al., 2014, *MNRAS*, 445, 3200
- Stark D. P. et al., 2015a, *MNRAS*, 450, 1846
- Stark D. P. et al., 2015b, *MNRAS*, 454, 1393
- Stark D. P. et al., 2017, *MNRAS*, 464, 469
- Steidel C. C., Strom A. L., Pettini M., Rudie G. C., Reddy N. A., Trainor R., 2016, *ApJ*, 826, 159
- Trainor R. F., Steidel C. C., Strom A. L., Rudie G. C., 2015, *ApJ*, 809, 89

Trainor R. F., Strom A. L., Steidel C. C., Rudie G. C., 2016, *ApJ*, 832, 171
Vanzella E. et al., 2016a, *ApJ*, 825, 41
Vanzella E. et al., 2016b, *ApJ*, 821, 27
Verhamme A., Orlitová I., Schaerer D., Izotov Y. I., Worseck G., Thuan T. X., Guseva N., 2017, *A&A*, 597, A13
Villar-Martín M., Tadhunter C., Clark N., 1997, *A&A*, 323, 21

Wisotzki L. et al., 2016, *A&A*, 587, A98
Yamada T. et al., 2012, *AJ*, 143, 79
Yang H. et al., 2017, *ApJ*, 844, 171
Zheng Z., Wallace J., 2014, *ApJ*, 794, 116

This paper has been typeset from a \TeX/L\AA\TeX file prepared by the author.